Exploring the amplied role of HCHO in the formation of HMS and O₃ during the co-occurring PM₂.₅ and O₃ pollution in a coastal city of southeast China

Youwei Hong[a,b,c,d,g*], Keran Zhang[a,b,d], Dan Liao[f], Gaojie Chen[a,b,c], Min Zhao[i], Yiling Lin[a,b,e], Xiaoting Ji[a,b,c], Ke Xu[a,b,g], Yu Wu[a,b,e], Ruilian Yu[e], Gongren Hu[e], Sung-Deuk Choi[h], Likun Xue[i*], Jinsheng Chen[a,b,c]

[a]Center for Excellence in Regional Atmospheric Environment, Key Lab of Urban Environment and Health, Institute of Urban Environment, Chinese Academy of Sciences, Xiamen, 361021, China

[b]Fujian Key Laboratory of Atmospheric Ozone Pollution Prevention, Institute of Urban Environment, Chinese Academy of Sciences, Xiamen, 361021, China

[c]University of Chinese Academy of Sciences, Beijing, 100049, China

[d]College of Resources and Environment, Fujian Agriculture and Forest University, Fuzhou 350002, China

[e]College of Chemical Engineering, Huaqiao University, Xiamen, 361021, China

[f]College of Environment and Public Health, Xiamen Huaxia University, Xiamen 361024, China

[g]School of Life Sciences, Hebei University, Baoding, 071000, China

[h]Department of Urban and Environmental Engineering, Ulsan National Institute of Science and Technology, Ulsan, 44919, South Korea

[i]Environment Research Institute, Shandong University, Qingdao, 266237, China

*Corresponding author E-mail: Youwei Hong (ywhong@iue.ac.cn); Likun Xue (xuelikun@sdu.edu.cn)

Abstract:

To develop the effective strategies for controlling both $PM_{2.5}$ and O_3 levels, it is crucial to understand their synergistic mechanisms, key precursors, and atmospheric physiochemical processes involved. In this study, a wintertime co-occurring O_3 and $PM_{2.5}$ pollution event in a coastal city in southeast China was investigated based on high-time resolution measurements of criteria air pollutants, chemical compositions of $PM_{2.5}$, and O_3 precursors, such as NOx, HCHO, and VOCs. The results of this study revealed the characteristics of positively correlated $PM_{2.5}$ and MDA8 O_3 concentrations, and an increase in atmospheric oxidation capacity (AOC) during the cold seasons. Strong correlations (R^2 = 0.415–0.477) between HCHO, Fe, Mn, and sulfate concentrations were observed, suggesting the influence of catalyzed oxidation processes in the coastal city. Through an observation-based model (OBM) analysis coupled with the regional atmospheric chemistry mechanism version 2 (RACM2) and the chemical aqueous-phase radical mechanism version 3.0 (CAPRAM 3.0), we found that high concentrations of precursors (SO_2 and HCHO), high relative humidity, and moderately acidic pH conditions enhanced the heterogeneous formation of hydroxymethanesulfonate (HMS) in $PM_{2.5}$. Furthermore, by employing the Master Chemical Mechanism (OBM-MCM), we verified that disabling the HCHO mechanism could decrease daytime net O_3 production rates by reducing the production rates of HO_2+NO. These results were consistent with the daily values of AOC, OH, HO_2, and RO_2 concentrations. This study contributes to a better understanding of the significance

50   of HCHO in photochemical reactions and the formation of HMS in coastal city.

51   **Key words:** $PM_{2.5}$; O_3; formaldehyde; OBM; coastal city

52

Introduction

54   Air pollution, dominated by fine particulate matter ($PM_{2.5}$) and ground-level ozone

55   (O_3), is an important global environmental issue linked to climate change and human

56   health, including cardiovascular and respiratory illnesses and mortality (Xiao et al.,

57   2022; Vohra et al., 2022). To decrease global air pollution and associated mortality, the

58   World Health Organization recently updated its air quality guideline for annual $PM_{2.5}$

59   exposure from 10 to 5 $\mu g\ m^{-3}$ and added the average O_3 concentrations of no more than

60   60 $\mu g\ m^{-3}$ during the peak season (WHO, 2021). To develop two-pollutant control

61   strategies to decrease both $PM_{2.5}$ and O_3, there is a need to understand the synergistic

62   mechanisms and spatiotemporal delineation between them (Ivatt et al., 2022; Li et al.,

63   2019b).

64   There are complex synergistic effects between $PM_{2.5}$ and O_3, due to common

65   precursors (e.g., NOx and VOCs), atmospheric physiochemical processes, and weather

66   systems (Li et al., 2019a; Shao et al., 2022; Jia et al., 2023; Zhang et al., 2022; Qin et

67   al., 2021; Qu et al., 2023). An increase in O_3 concentration will increase oxidizing

68   substances, such as OH, H_2O_2, and RCHO, which promote the oxidation of SO_2, NOx,

69   and VOCs to secondary inorganic and organic components in $PM_{2.5}$ (Feng et al., 2020;

70   Lu et al., 2019). On the contrary, multiphase reactions occur on the surface of

71   atmospheric particles, such as the uptake of HCHO and HO_2 absorption, thus affecting

72   the formation of O_3 (Song et al., 2022; Lou et al., 2014).

73   Formaldehyde (HCHO) plays an important role in the photochemical reaction

74   process and secondary aerosol formation (Kalashnikov et al., 2022; Ma et al., 2020;

75   Song et al., 2021; Zong et al., 2021). Most studies have focused on pollution

76   characteristics and sources, particle uptake of HCHO, and their impacts on atmospheric

77   oxidation capacity (Liu et al., 2022b; Wu et al., 2023; Zhang et al., 2021). Recent

78   studies have shown that HCHO can react with hydrogen peroxide (H_2O_2) to produce

79   hydroxymethyl hydroperoxide (HMHP), which rapidly oxidizes dissolved sulfur

80   dioxide (SO_2, aq) to sulfate (Dovrou et al., 2022). Meanwhile, HCHO reacts with

81   dissolved SO_2 (aq) to produce hydroxymethanesulfonate (HMS, $HOCH2SO−$), which,

82   upon oxidation with the hydroxyl radical (OH), forms sulfate (Ma et al., 2020; Moch et

83   al., 2018, 2020). Totally, atmospheric HCHO contributes to sulfate formation in $PM_{2.5}$

84   by producing HO_2 radicals and HMHP or HMS (Wu et al., 2023; Dovrou et al., 2022;

85   Campbell et al., 2022). However, these studies highlight the necessity for more

86   observation research to obtain evidence of the contributions of HCHO to HMS

87   formation. HMS is an important organosulfur compound in the atmosphere, not only in

88   cloud and fog but also in atmospheric aerosols (Munger et al., 1986; Dixon and Aasen,

89   1999). The misidentification of HMS as inorganic sulfate caused the overestimation of

90   the observed particulate sulfate (Ma et al., 2020; Dovrou et al., 2022). However, in

91   subtropical coastal regions with apparent HCHO production, further studies are

92   required to investigate the impacts of HCHO on the the formations of HMS and ROx

93 radicals.

94   Xiamen, a coastal city in southeast China, has frequently experienced $PM_{2.5}$

95 pollution (with low O_3 concentrations) in winter and O_3 pollution in spring and autumn

96 (Hong et al., 2022; Wu et al., 2019). Our previous studies mainly focused on the

97 pollution characteristics of $PM_{2.5}$ or O_3 in different seasons and their sources associated

98 with anthropogenic emissions and the East Asian monsoon (Liu et al., 2020; Liu et al.,

99 2022a; Hong et al., 2021). At the end of winter and the beginning of spring in 2022, an

100 outbreak of co-occurring O_3 and $PM_{2.5}$ pollution was observed in Xiamen. Therefore,

101 it provided a unique opportunity to study the impacts of HCHO on the formations of

102 HMS and ROx radicals. In the coastal region, there is an apparent alternation of polluted

103 and clean air masses from continental and ocean areas and a local geographical

104 environment, including relatively high humidity, dense vegetation, and strong

105 atmospheric oxidation capacity (Hu et al., 2022; Wu et al., 2020). Potential roles and

106 mechanisms of HCHO in the photochemical reaction process and HMS formation

107 would differ from those in megacities of China, such as the Beijing-Tianjin-Hebei (BTH)

108 Area, the Yangtze River Delta (YRD), and the Pearl River Delta (PRD). Based on the

109 observation-based model (OBM) analysis, the objectives of this study are to (1)

110 characterize the wintertime co-occurring O_3 and $PM_{2.5}$ pollution process in a coastal

111 city; (2) elaborate the influence of HCHO on the heterogeneous formation of HMS in

112 $PM_{2.5}$; (3) explore the mechanisms of HCHO on O_3 pollution and photochemical

113 reactions process.

114

2 Methods and materials

2.1 Study area

The monitoring site (Institute of Urban Environment, Chinese Academy of Sciences, 118.06° E, 24.61° N) is located in Xiamen, a coastal city in southeast China (Fig. S1). It is situated in a subtropical monsoon climate, with an average temperature of 18.5°C and a relative humidity of 63.3% during the wintertime observation. In autumn and winter, cold and dry air masses move northward from inland, while in late spring and summer, the prevailing air masses are southerly, characterized by warm air temperatures and high humidity. The air-monitoring supersite is located on the rooftop of a building, surrounded by residential buildings, educational institutions, a commercial zone, and freeways. The downtown area of Xiamen, with a high population density and frequent traffic jams, is located south of the monitoring site.

2.2 Observation

Gas and aerosol species, O_3 precursors, photolysis rate, and meteorological parameters were continuously measured online from February 17 to March 17, 2022. Hourly mass concentrations of $PM_{2.5}$ and PM_{10} were measured using a tapered element oscillating microbalance (TEOM1405, Thermo Scientific Corp., MA, USA). NO/NO_2, SO_2, and O_3 were monitored using continuous gas analyzers (TEI 42i, 43i, and 49i, Thermo Scientific Corp., MA, USA). HCHO analyzer (FMS-100, Focused Photonics Inc., Hangzhou, China) was used to measure gaseous HCHO based on the Hantzsch

136   reaction, according to our previous method (Liu et al., 2022b). Water-soluble inorganic

137   ions (WSII) in $PM_{2.5}$ (Cl^-, SO_4^{2-}, NO_3^-, Na^+, K^+, NH_4^+, Mg^{2+}, and Ca^{2+}) were measured

138   hourly using a Monitoring device for AeRosols and Gases in ambient Air (MARGA

139   2080; Metrohm Applikon B.V.; Delft, Netherlands). Simultaneously, organic carbon

140   (OC) and elemental carbon (EC) in $PM_{2.5}$ were measured using an OC/EC analyzer

141   (model RT-4; Sunset Laboratory Inc.; Tigard, USA). BC was monitored using an

142   Aethalometer (AE31, Magee Scientific, USA) with a $PM_{2.5}$ cut-off inlet. Besides,

143   concentrations of 22 elements (Al, Si, S, Fe, K, Mn, Pb, Ca, Zn, Ba, V, Cu, Ni, As, Cr,

144   Ag, Se, Br, Hg, Sn, Ti, and Sb) were measured using a multi-metal monitor (Xact™

145   625, Cooper Environmental Services, LLT; Portland, USA). Strict quality assurance

146   and quality control procedures were applied, and the maintenance and accuracy of all

147   online instruments were validated (Hong et al., 2021). The detection limits, time

148   resolutions and measured uncertainties of air pollutants were shown in TableS3.

149   A gas chromatograph-mass spectrometer (GC-FID/MS, TH-300B, Wuhan, China)

150   was used to measure ambient VOCs with one-hour time resolution, following the

151   method from our previous studies (Liu et al., 2020a,b). Briefly, the air sample was

152   preconcentrated by cooling to −160 °C in a cryogenic trap, then heated to 100 °C, and

153   subsequently transferred to the secondary trap using high-purity helium (He). The low-

154   carbon (C2-C5) hydrocarbons were detected using a flame ionization detector (FID)

155   with a PLOT (Al_2O_3/KCl) column (15 m × 0.32 mm × 6.0 μm), while other VOC

156   species were quantified using a GC/MS with a DB-624 column (60 m × 0.25 mm × 1.4

157   μm). The instrument can quantify 106 VOC species, including 29 alkanes, 11 alkenes,

158 one alkyne, 17 aromatics, 35 halogenated hydrocarbons, and 13 OVOCs. Calibration

159 was performed daily at 11:00 pm using the standard mixtures of US EPA PAMS and

160 TO-15. The detection limits of the measured VOCs ranged from 0.02 ppbv to 0.30 ppbv.

161 Ambient meteorological parameters, including relative humidity (RH),

162 temperature (T), wind speed (WS), and wind direction (WD), were obtained using an

163 ultrasonic atmospherium (150WX, Airmar, USA). Photolysis frequencies and HCHO

164 were measured using a photolysis spectrometer PFS-100 and a formaldehyde monitor

165 FMS-100 (Focused Photonics Inc., Hangzhou, China), respectively. The photolysis rate

166 constants include $J(O^1D)$, $J(NO_2)$, $J(H_2O_2)$, $J(HONO)$, $J(HCHO)$, and $J(NO_3)$. The

167 distribution of fire spots during the observation periods was obtained from the Fire

168 Information for Resource Management System

169 (https://firms.modaps.eosdis.nasa.gov/firemap/). The data for boundary layer height

170 (BLH) were obtained from the European Centre for Medium-Range Weather Forecasts

171 (ECMWF) ERA5 hourly reanalysis dataset

172 (https://www.ecmwf.int/en/forecasts/datasets/reanalysis-datasets/era5, last access:

173 March 24, 2023). The resolution of ERA-5 reanalysis is 0.25°×0.25°.

174

175 **2.3 Positive matrix factorization (PMF) analysis**

176 The PMF 5.0 model was applied to quantify high-time-resolution sources of $PM_{2.5}$

177 during the observation periods. The details of the model analysis were described in our

178 previous studies (Hong et al., 2021; Liu et al., 2020). Briefly, Eq. (1) demonstrates j

179 compound species in the ith sample as the concentration from p independent sources.

$$x_{ij} = \sum_{k=1}^{p} g_{ik} f_{ki} + e_{ij}$$

(1)

Where e_{ij} is the residual for each species, f_{kj} is the fraction of the jth species from the kth source, g_{ik} is the species contribution of the kth source to the ith sample, x_{ij} is the jth species concentration measured in the ith sample, and p is the total number of independent sources. The Q value (Eq. (2)), based on the uncertainties (μ), was used to evaluate the steadiness of the solution.

$$Q = \sum_{i=1}^{n} \sum_{j=1}^{m} \left[\frac{x_{ij} - \sum_{k=1}^{p} g_{ik} f_{kj}}{\mu_{ij}} \right]^2$$

(2)

2.4 Observation-based model (OBM)

The OBM-MCM model is employed to simulate in situ atmospheric photochemical processes and quantify the O_3 production rate, AOC, and OH reactivity. The details of the OBM-MCM model were reported in our previous studies (Liu et al., 2022a,b). In summary, monitoring data with a one-hour time resolution of air pollutants (i.e., O_3, CO, NO, NO_2, HONO, SO_2, and VOCs), meteorological parameters (i.e., T, P, and RH), and photolysis rate constants ($J(O^1D)$, $J(NO_2)$, $J(H_2O_2)$, $J(HONO)$, $J(HCHO)$, and $J(NO_3)$) were input into the OBM-MCM model as constraints for the model simulation. The photolysis rates of other molecules were determined by solar zenith angle and scaled using measured $J\!NO_2$ values (Saunders et al., 2003). According to our previous studies, the model incorporates the physical process of deposition within the boundary layer height (BLH), which varies from 300 m during nighttime to 1500 m

during the daytime in winter (Li et al., 2018;Liu et al., 2022). Therefore, dry deposition velocities were used to simulate the deposition loss of certain reactants in the atmosphere (Zhang et al., 2003; Xue et al., 2014).

To simulate the concentration of particulate HCHO and its role in the heterogeneous formation of hydroxymethanesulfonate (HMS), the observation-based zero dimensional multiphase chemical box model was used, of which the gas phase chemistry is described by he regional atmospheric chemistry mechanism version 2 (RACM2) and the aqueous phase part of the mechanism is represented by the chemical aqueous-phase radical mechanism version 3.0 (CAPRAM 3.0). The mass transfer processes between the gas and aqueous phases is also considered in current model according to Schwartz (1986). The Henry's law constant of HCHO was updated with a value of 0.31×10^8 M atm^{-1}, as estimated by Mitsuishi et al. (2018). Sensitivity analysis was conducted to evaluate the uncertainties introduced by the Henry's law constant, details can be found in SI. For major production and loss paths of HMS, dissolved HCHO reacts with sulfite and bisulfite to form HMS (Eq (3-4)), which can be further oxidized by aqueous OH radicals (Eq (5)), details about the HMS mechanisms and the corresponding reaction kinetics are documented in CAPRAM website (https://capram.tropos.de/).

$$HCHO_{(aq)} + HSO_3^- = HOCH_2SO_3^- \tag{3}$$

$$HCHO_{(aq)} + SO_3^{2-} + H_2O = HOCH_2SO_3^- + OH^- \tag{4}$$

$$HOCH_2SO_3^- + OH \cdot = 2SO_4^{2-} + HCHO_{(aq)} + 3H^+ \tag{5}$$
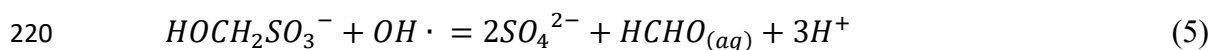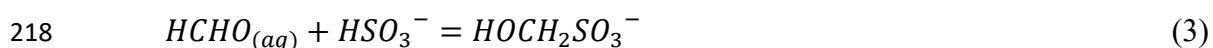
221   For detailed modeling steps of HMS, firstly, the observation data of gaseous NO,

222   NO_2, O_3, SO_2, CO, NMHCs, HCHO and other ten carbonyls, particulate phase NO_3^-,

223   NH_4^+, and Cl^-, along with meteorological parameters were averaged or interpolated into

224   a 1-h time resolution and classified into model recognized groups as model inputs,

225   while the measured SO_4^{2-} was used as the initial conditions. Liquid water content (LWC)

226   and aqueous H^+ concentrations, calculated using the ISORROPIA-II model (Hong et

227   al., 2022), were also used as model inputs. Then, model calculations were conducted

228   using the commercial FACSIMILE software, the modeling period was from February

229   26 to March 16, 2022 and each day was regarded as an independent simulation case.

230   The model was constrained every hour by the input observation data for integral

231   calculation. For each case, The integration ran three times in series to steady the

232   unconstrained species (e.g., radicals) , which was initiated at 00:00 local time (LT), and

233   had a step of 1 h and a duration of 24 h. Finally, the modeled HMS concentrations of

234   the third run were outputted with a 1-hour time resolution for further analysis.

235

3 Results and discussions

236

3.1 Overview of co-occurring O_3 and $PM_{2.5}$ pollution

237

238   The time series of criteria air pollutants, O_3 precursors, and meteorological

239   parameters from February 17 to March 17, 2022 are shown in Fig. 1. Two typical $PM_{2.5}$

240   and O_3 pollution episodes (EP1: February 26 to March 5; EP2: March 11 to March 17)

241   were observed, compared to the other periods (Pre-EP1: February 11 to February 25

242 and Pre-EP2: March 16 to March 10) affected by rainfall. The mean concentrations of

243 $PM_{2.5}$ during EP1 and EP2 were 51.9 μg m^{-3} and 35.3 μg m^{-3}, respectively, compared

244 to 9.03 μg m^{-3} during Pre-EP1 (Table S1). The concentrations of other air pollutants,

245 such as O_3, SO_2, NO_2, PM_{10}, OC, EC, BC, HCHO, and VOCs, showed a significant

246 increasing trend during EP1 and EP2. During the monitoring periods, the

247 concentrations of measured HCHO ranged from 0.68 ppbv and 3.59 ppbv (Tabe S1).

248 According to our previous studies (Liu et al., 2023), the average levels of the measured

249 HCHO in spring and autumn in Xiamen were 2.9 ± 0.3 ppbv and 3.2 ± 1.4 ppbv,

250 respectively. Totally, the HCHO level in Xiamen was lower than that in megacities

251 (Table S2), such as Beijing (summer: 11.39±5.58 ppbv), Hongkong (summer:

252 8.07±1.94 ppbv), and Guangzhou (summer: 6.69±1.98 ppbv), while was comparable to

253 the coastal cities, including Shenzhen (spring: 3.4±1.6 ppbv), Yantai (summer:

254 3.90±1.12 ppbv), and Shanghai (summer:3.31±1.43 ppbv). In the coastal cities of

255 southeastern China, halogenated VOC is one of important VOC species, which

256 originated from industrial emissions and solvent usage (Chen et al., 2022; Ji et al., 2022;

257 Liu et al., 2022). In this study, during the monitoring period, backward trajectories

258 showed air mass transport from the northeast, which brought halogenated VOC from

259 Quanzhou city, an industrial city adjacent to Xiamen.

260 The maximum $PM_{2.5}$ and O_3 concentrations were approximately 100 μg m^{-3} and

261 200 μg m^{-3}, respectively. The maximum daily 8 h average (MDA8) O_3 concentrations

262 were calculated according to the Ambient Air Quality Standard of China. Fig. S2 shows

263 the positive correlation between $PM_{2.5}$ and MDA8 O_3 concentrations during the whole

264   period. In Xiamen, a coastal city in Southeast China, the annual mean concentrations

265   of criteria air pollutants from 2015 to 2021 were significantly lower than in other

266   Chinese cities (Fig. S3) (Li et al., 2022; Shao et al., 2022). Meanwhile, inter-annual

267   averaged concentrations of O_3 and Ox in winter were shown in Fig S3, suggesting an

268   increase in atmospheric oxidation capacity (AOC) during the cold seasons. Therefore,

269   these two typical $PM_{2.5}$ and O_3 pollution episodes (EP1 and EP2) are worth exploring

270   in terms of the formation mechanisms and synergistic effects of $PM_{2.5}$ and O_3 in the

271   coastal city.
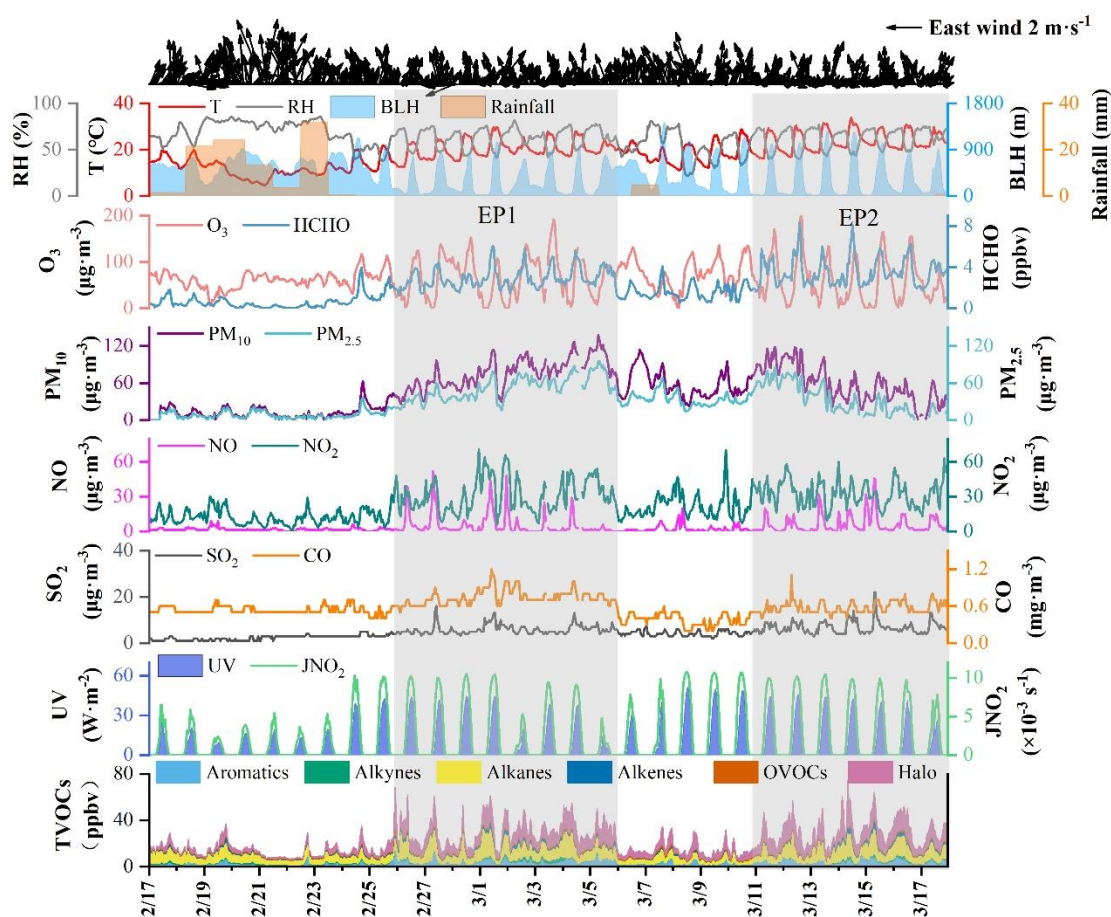
272

273   **Fig. 1. Time series of various air pollutants and meteorological parameters**

274

3.2 Chemical compositions and sources of PM$_{2.5}$

As shown in Figure 2, an overall increasing trend is clearly observed in both bulk PM$_{2.5}$ and its major components during EP1 and EP2. Nitrate and organic matter (OM) remain the top two dominant PM$_{2.5}$ components, followed by sulfate and ammonium. The mean concentrations of SO$_4^{2-}$, NO$_3^-$, and NH$_4^+$ during EP1 and EP2 were 7.07 μg m^{-3} and 5.87 μg m^{-3}, 14.95 μg m^{-3} and 9.69 μg m^{-3}, and 6.77 μg m^{-3} and 4.46 μg m^{-3}, respectively (Table S1). The increase in EC indicates the contributions of local anthropogenic emission sources, such as vehicle exhausts (Fig. 2). The concentrations and percentages of OC and EC during different periods are illustrated in Fig. S4 and Table S1. The average OC and EC concentrations during EP1 and EP2 were 6.36 μg m^{-3} and 7.48 μg m^{-3} and 1.23 μg m^{-3} and 1.29 μg m^{-3}, respectively, which were notably higher than those during Pre-EP1 and Pre-EP2. These results are consistent with the increase in primary emissions and secondary formation contributing to complex air pollution during the rapid urbanization and industrialization stages in China (Xiao et al., 2022; Jiang et al., 2022).

290
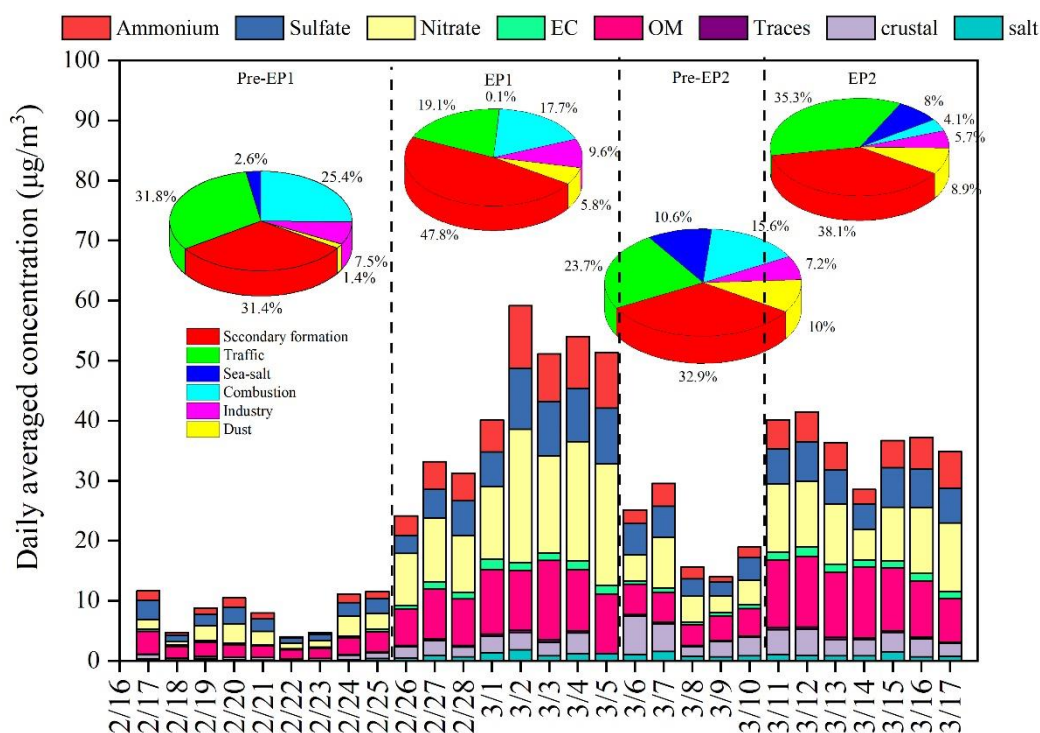
Fig. 2. Time series of PM$_{2.5}$ chemical composition and sources apportionment by the PMF model. In the legends, OM refers to organic matter, calculated as 1.4×OC; "Tracers" includes elements other than Na, Cl, S, K, Al, Si, Ca, Fe; "Crustal" represents crustal materials, calculated as 1.89×Al+2.14×Si+1.4×Ca+1.43×Fe; and "Salts" includes Na$^+$ and Cl$^-$.

The PMF model was applied to conduct high-time-resolution source apportionment of PM$_{2.5,}$ based on online hourly measurement data (Hong et al., 2021; Chow et al., 2022). The factor profiles and the contributions of various sources to PM$_{2.5}$ are shown in Fig. 2 and Fig. S5. Previous studies have indicated that construction and road dust is characterized by high loadings of Al, Si, Ca^{2+}, Na$^+$, Mg^{2+}, and Zn (Rienda and Alves, 2021). In this study, the factor of dust (Factor 1) was identified by the high contributions of Si (Fig. S5). The PMF analysis revealed that the contribution of dust to PM$_{2.5}$ ranged from 5.8% to 8.9% during EP1 and EP2, compared to 1.4% during Pre-EP1 (Fig.2). Factor 2, contributing to the high loading of metal elements (Mn, Zn, Fe, Pb, and As), was characterized by industrial emissions (Belis et al., 2019). The

305   contributions from the industry during EP1 and EP2 remained constant. In factor 3, K^+

306   was dominant, and it was identified as coming from combustion sources (Watson et al.,

307   2001). Biomass burning could change the contribution of combustion to $PM_{2.5}$ at the

308   monitoring site through long-range transport. During EP2, the influence of combustion

309   sources (e.g., biomass burning) significantly decreased, due to reduced anthropogenic

310   emissions and the arrival of clean air masses from the ocean (Figs. S6 and S7). Factor

311   4, with the highest proportion of Na^+ and Mg^{2+} loadings, was associated with the

312   influence of sea-salt aerosol (Polissar et al., 1998). The percentages of sea salt (8-10%)

313   during Pre-EP2 and EP2 were relatively high. Factor 5 exhibited high contributions of

314   EC, OM, and Pb, which are general indicators of vehicle exhaust (Belis et al., 2019).

315   During EP2, the contribution of traffic increased up to 35.3%. Factor 6 was associated

316   with secondary aerosol, characterized by high loadings of SO_4^{2-}, NO_3^-, and NH_4^+. The

317   increased contributions of secondary formation during EP1 and EP2 accounted for 47.8%

318   and 38.1%, respectively.

319

320   **3.3 Formation mechanism of $PM_{2.5}$**

321   As shown in Fig. S8, SO_4^{2-} was correlated with NH_4^+ (R^2 = 0.72–0.88), and the

322   line fit of NH_4^+ and SO_4^{2-} showed a slope of 1.78-2.67, suggesting the dominant form

323   of $(NH_4)_2SO_4$. Similarly, NO_3^- was also correlated with NH_4^+ (R^2 = 0.77–0.93),

324   indicating the presence of NH_4NO_3. In addition, the ratio of NH_4^+ to the sum of NO_3^-

325   and SO_4^{2-} was close to 1, indicating complete neutralization of sulfate and nitrate by

326   ammonium (Fig. 8c). However, there was no significant difference in the existing form

327   of SNA in $PM_{2.5}$ during EP1 and EP2.

328   The variations of sulfur oxidation rate (SOR) and nitrogen oxidation rate (NOR)

329   under different periods are shown in Table S1. It should be noted that SOR (0.38±0.18)

330   and NOR (0.32±0.08) during EP1 were the highest, indicating a high oxidation rate of

331   SO_2 and NO_2. According to RH, T, and UV (Table S1), noticeable differences in

332   meteorological conditions were observed under different periods. In this study, LWC

333   was positively correlated with SO_4^{2-}, NO_3^-, and NH_4^+ (known as the secondary

334   inorganic aerosol, SIA) (Fig. S9), suggesting the influence of the aqueous phase process,

335   including reactions with O_3, OH, H_2O_2, and organic peroxides (Gen et al., 2019; Wang

336   et al., 2023).

337   Current studies have found that O_3, H_2O_2, OH, and transition-metal-catalyzed

338   (TMI) O_2 can trigger the secondary formation of SO_4^{2-} (Hong et al., 2021; Gen et al.,

339   2019). However, the relative importance of these oxidants in enhancing the formation

340   of SO_4^{2-} is still a topic of debate. As shown in Fig. 3(b) and (c), a good correlation was

341   found between SO_4^{2-} and Fe and Mn. The TMI-catalyzed oxidation contributed to the

342   formation of SO_4^{2-}, which occurred in both cloud processes and during haze episodes

343   (Li et al., 2020) because the Mn catalytic reaction rapidly occurred at the aerosol surface

344   and could oxidize S(IV) through the production of intermediate Mn(III) (Wang et al.,

345   2021). Even at very low concentrations of Mn, the Mn catalytic reaction, consuming

346   oxygen and SO_2, could produce sulfate. Under low aerosol pH conditions, the catalytic

347   reaction of TMIs plays an important role in the oxidation of S(IV). In this study, low

348   aerosol pH ranged from 2 to 4 was observed, indicating the potential influence of TMI-

349 catalyzed oxidation. In the future, it is vital to further evaluate the interaction of sulfate

350 formation and Fe/Mn, and to elucidate the main pathway of the S(IV) oxidation in the

351 coastal areas. In addition, as an important intermediate product in atmospheric

352 photochemical reactions, the formation and removal of HCHO are closely related to

353 OH and HO_2 radicals, which directly affect atmospheric reactivity and oxidation ability

354 (Wu et al., 2023; Zhang et al., 2021). In this study, the correlations ($R^2 = 0.415$) between

355 HCHO and sulfate concentrations were also examined, as displayed in Fig. 3(a). Recent

356 studies have shown that HCHO can react with hydrogen peroxide (H_2O_2) to produce

357 hydroxymethyl hydroperoxide, which rapidly oxidizes dissolved sulfur dioxide (SO_2,

358 aq) to sulfate (Dovrou et al., 2022).
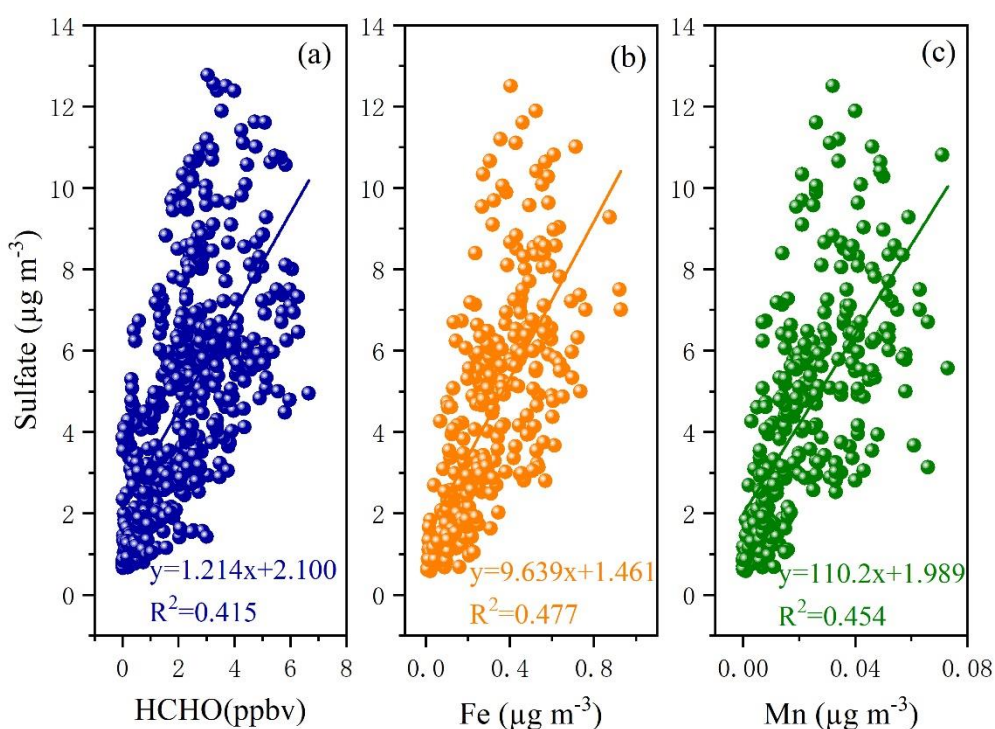
359

360 **Fig.3. Correlations between the concentrations of sulfate and HCHO (a), Fe (b), and Mn (c)**

361

3.4 Effects of HCHO on HMS in PM$_{2.5}$

To calculate the particulate concentrations of HCHO and its contributions to the heterogeneous formation of HMS, we conducted the in-situ multiphase chemical simulations by combining the zero dimensional multiphase chemical box model with RACM2 and CAPRAM 3.0. During EP1 and EP2, the concentrations of HCHO (aq) and HMS (aq), as well as the particulate sulfur molar percentage, increased with the rise of SO$_2$, SO$_4^{2-}$, and HCHO concentrations (Fig. 4). Also, particulate sulfur molar percentage was higher during the pollution periods, which may due to the high concentrations of gaseous precursors (SO$_2$, HCHO) and favorable aerosol properties (i.e. pH and aerosol water content) promoted the heterogeneous processes. Previous studies have modeled that 1 ppb of gas-phase HCHO could yield up to ~5 μg m^{-3} HMS and identified that HCHO emissions was one of key factors controlling HMS formation during the winter haze (Moch et al., 2018). All above signify the important contributions of HCHO on the heterogeneous formation of HMS and particulate sulfur chemistry, especially during the pollution periods.

However, the molar ratio of HMS to sulfate were very low, suggesting the limited contributions of HMS concentrations to inorganic sulfate concentrations. Potential roles of HCHO in the HMS formation in coastal city of southeast China was differed from those in the megacities of China. Previous studies found that HCHO reacts with dissolved SO$_2$ (aq) to produce hydroxymethanesulfonate (HMS), which, upon oxidation with the hydroxyl radical (OH), forms sulfate (Ma et al., 2020; Moch et al., 2020). Ma et al. (2020) reported that heterogeneous formation of HMS accounted for

384   15% of OM, and resulted in 36% overestimates of sulfate during the winter haze in

385   Beijing.
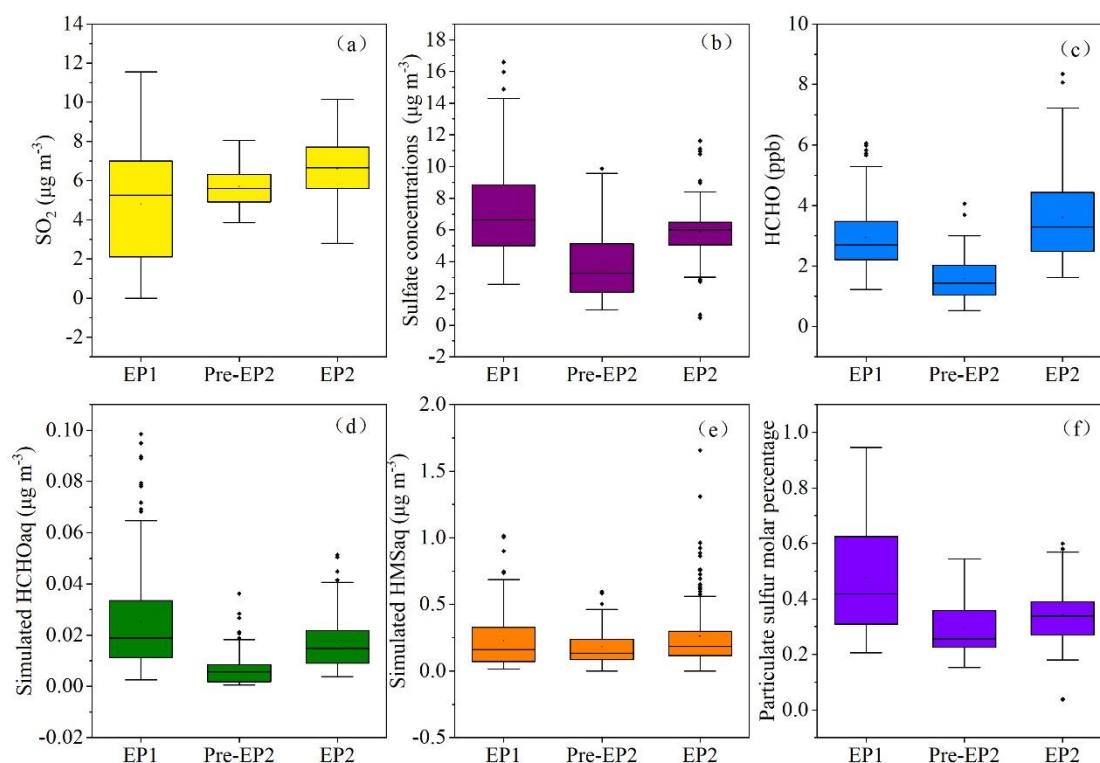
386

387   **Figure 4. Concentrations of SO$_2$, SO$_4^{2-}$, and HCHO observed at different pollution stages.**
388   **The simulated HCHO (aq) and HMS (aq) were also presented. The particulate sulfur molar**
389   **percentage was calculated as [n(SO$_4^{2-}$)+n(HMS)]/[n(SO$_4^{2-}$)+n(HMS)+ n(SO$_2$)]. In the box–**
390   **whisker plots, the whiskers, boxes, and points indicate the 5th/95th, 25th/75th, 50th percentiles,**
391   **and mean values.**

392   High concentrations of HMS were captured under high RH and moderately acidic

393   pH conditions (Fig. 5). Previous studies have also indicated that high RH promotes

394   rapid HMS formation during winter haze, as the aerosol water content could provide

395   numerous reaction interfaces for HMS formation (Ma et al., 2020). Meanwhile,

396   atmospheric sulfur tended to distribute into the particle phase with increasing RH. Fig.

397   5 shows that HMS formation is favored under pH conditions close to 4.0. Previous

398   studies reported that high HMS concentrations were found under moderate-pH

399 conditions, as low pH inhibits HMS formation, and high pH is unsuitable for its

400 preservation (Ma et al., 2020; Campbell et al., 2022). Therefore, the combination of

401 high precursor concentrations (SO_2 and HCHO), high RH, and moderately acidic pH

402 enhanced the heterogeneous formation of HMS in the coastal city.

403
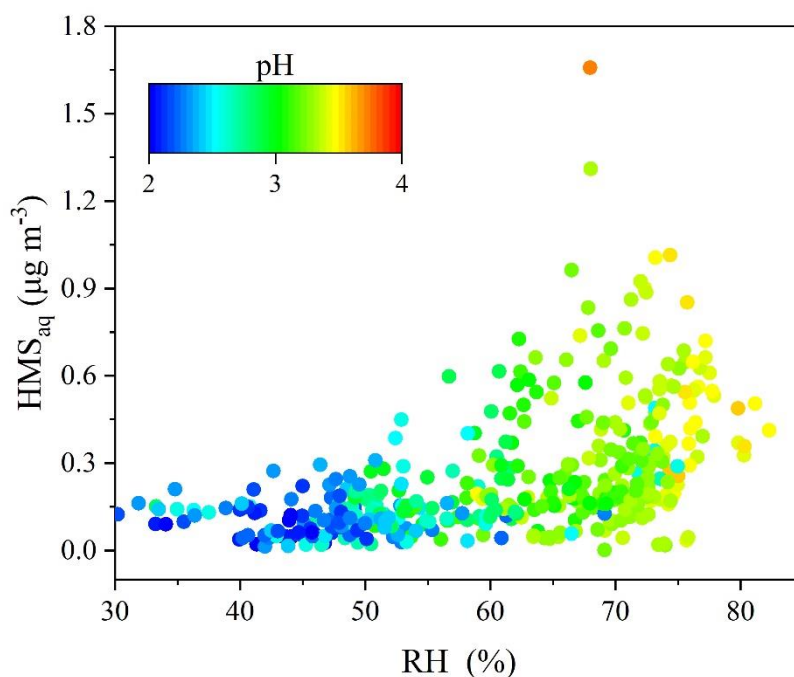
Figure 5. Evolution of HMS (aq) distribution with increasing RH, colored according to aerosol pH.

406

3.5 Effects of HCHO on O_3 formation

408   To investigate the effects of HCHO on O_3 formation during the co-occurring O_3

409 and $PM_{2.5}$ pollution period, the OBB was used to quantify the detailed O_3 production

410 and loss pathways in both scenarios: input HCHO (IH) and non-input HCHO (NIH)

411 (Fig. 6 and Fig. S9). The daytime production rates of HO_2+NO and RO_2+NO in the IH

412 scenario were calculated to be 6.84 and 1.25 ppbv h^{-1} for EP1 and 9.91 and 2.17 ppbv

413 h^{-1} for EP2, respectively. Meanwhile, the predominant O_3 loss reaction in this scenario

was OH+NO$_2$, with rates of 2.26 ppbv h^{-1} for EP1 and 3.17 ppbv h^{-1} for EP2, followed

by O$_3$ photolysis with rates of 0.77 ppbv h^{-1} and 1.10 ppbv h^{-1}. In contrast, the daytime

production rates of HO$_2$+NO and RO$_2$+NO in the NIH scenario were 4.03 and 0.85

ppbv h^{-1} for EP1 and 4.86 and 1.29 ppbv h^{-1} for EP2, respectively. These results

indicate that disabling the HCHO mechanism reduced the production rates of HO$_2$+NO

by 41% for EP1 and 51% for EP2. In addition, the average maximum net O$_3$ production

rate with the IH scenario was 5.02 ppb h^{-1} for EP1 and 7.93 ppb h^{-1} for EP2,

approximately two times higher than the values of 2.48 ppb h^{-1} and 3.14 ppb h^{-1} with

the NIH scenario. The results showed that the daytime net O$_3$ production rates decreased

by 50–60% when the HCHO mechanism was disabled, probably due to the decrease in

ROx concentrations and radical propagation rates (Wu et al., 2023; Zhang et al., 2021).
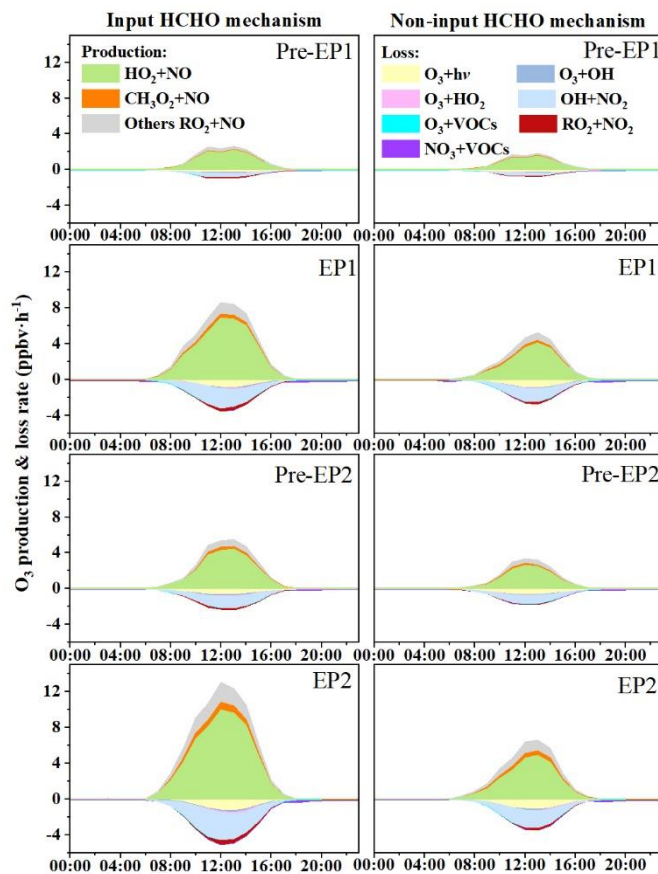
426 **Figure 6. O_3 production and loss rates by the OBM with and without the HCHO mechanism**

427   The atmospheric oxidation capacity (AOC) is a critical factor in determining the

428 production rate of secondary pollutants and atmospheric photochemical pollution (Jia

429 et al., 2023; Qin et al., 2022). In this study, AOC is calculated as the sum of the oxidation

430 rates of various primary pollutants (e.g., CO, NOx, and VOCs) by major oxidants (i.e.,

431 OH, O_3, and NO_3). The model-simulated AOC, OH, HO_2, and RO_2 under different

432 periods are shown in Fig. 7 and Fig. 8. The daily maximum AOC during EP1 and EP2

433 was 8.24×10^7 and 11.6×10^7 molecules cm^{-3} s^{-1}, respectively, which were higher than

434 those (2.56×10^7 and 5.39×10^7 molecules cm^{-3} s^{-1}) in other periods. However, when the

435 HCHO mechanism was disabled, the daily maximum AOC during different stages

436 decreased significantly. Especially, HCHO played much important role in AOC during

437 the co-occuring $PM_{2.5}$ and O_3 pollution periods. All these results are comparable to rural

438 sites in Hong Kong (6.2×10^7) and Berlin (1.4×10^7 molecules cm^{-3} s^{-1}) but lower than

439 those observed in highly polluted cities, such as Santiago (3.2×10^8 molecules cm^{-3} s^{-1})

440 and Shanghai (1.0×10^8 molecules cm^{-3} s^{-1}) (Li et al., 2018; Xue et al., 2016; Liu et al.,

441 2022a). These studies have reported that the variations in AOC are related to precursor

442 concentrations/types and photochemical conditions.

443
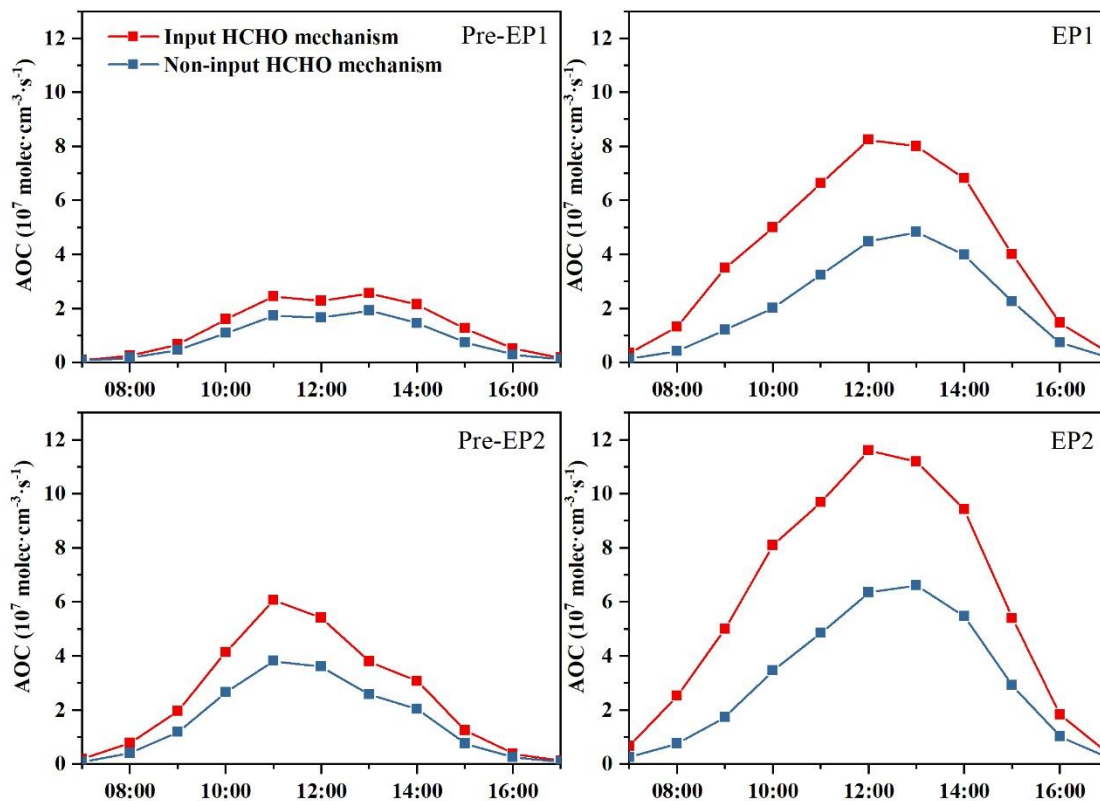
Figure 7. Atmospheric oxidation capacity (AOC) calculated by the OBM with and without the HCHO mechanism.

In addition, the maximum daily concentrations of OH, HO_2, and RO_2 exhibited a similar pattern to that of AOC in both the IH and NIH scenarios (Fig. 8). Therefore, the O_3 production rate during EP1 and EP2 was consistent with the maximum daily values of AOC, OH, HO_2, and RO_2. The differences in ROx levels between the IH and NIH model scenarios were also calculated (Fig. S10). In this study, disabling the HCHO mechanism led to decreased ROx concentrations, affecting the O_3 formation. These results highlight the significance of HCHO in the photochemical reactions occurring in the coastal city during the co-occurring O_3 and $PM_{2.5}$ pollution events.

454
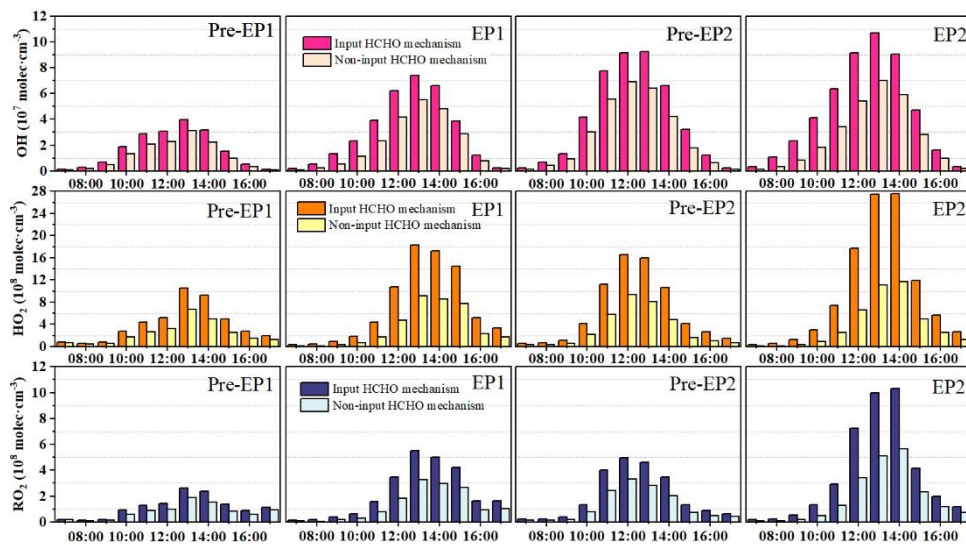
Figure 8. OH, HO₂, and RO₂ concentrations modeled by the OBM with or without the HCHO mechanism

455
456
457
458

459

Conclusions

A wintertime co-occurring O_3 and $PM_{2.5}$ pollution event was selected to investigate the synergistic effects between $PM_{2.5}$ and O_3 in a coastal city in southeast China. The results domonstrated a positive correlation between $PM_{2.5}$ and MDA8 O_3 concentrations during the whole periods, indicating the enhancement of atmospheric oxidation capacity (AOC) during cold seasons. The result of positive matrix factorization (PMF) analysis suggested that the contribution of secondary formation to $PM_{2.5}$ increased during the pollution events, implying that the elevated AOC promoted the oxidation of SO_2, NOx, and VOCs, leading to the formation of secondary inorganic and organic components. We also found the significant correlations ($R^2 = 0.415–0.477$) between HCHO, Fe, Mn, and sulfate concentrations, suggesting the influence of catalyzed oxidation in the coastal city. Through OBM analysis, we demonstrated that high concentrations of precursors (SO_2 and HCHO), high RH, and moderately acidic pH conditions enhanced the heterogeneous formation of hydroxymethanesulfonate (HMS). Meanwhile, we verified that the input HCHO mechanism increased the concentrations of ROx and net O_3 production rates. Moreover, the production rates of HO_2+NO and RO_2+NO were enhanced, indicating that HCHO affected O_3 formation by controlling the efficiencies of radical propagation. This study highlighted the influence of the HCHO mechanism on photochemical reactions and the formation of HMS in $PM_{2.5}$ in coastal cities and was beneficial for improving air quality and protecting public health.

481

Data Availability. The data set related to this work can be accessed via https://doi.org/10.5281/zenodo.7799302 (Hong, 2023). The details are also available upon request from the corresponding author (ywhong@iue.ac.cn).

Authorship Contribution Statement. Youwei Hong designed and wrote the manuscript. Yiling Lin and Dan Liao collected the data. Gaojie Chen and Min Zhao contributed to the modeling analyses. Keran Zhang, Xiaoting Ji, Ke Xu and Yu Wu performed data analysis. Sung-Deuk Choi, Likun Xue, Ruilian Yu and Gongren Hu contributed to revising the manuscript. Jinsheng Chen supported funding of observation and researches.

Competing interests. The authors declare that they have no conflict of interest.

Acknowledgement. The authors gratefully acknowledge Yanting Chen and Zhiqian Shao (Institute of Urban Environment, Chinese Academy of Sciences) for their guidance and assistance during the observation, and Lingling Xu, Mengren Li, and Xiaolong Fan (Institute of Urban Environment, Chinese Academy of Sciences) for the discussion of this paper. This research was supported by the Xiamen Atmospheric Environment Observation and Research Station of Fujian Province (Institute of Urban Environment, Chinese Academy of Sciences).

Financial support. This research was financially supported by the National Natural Science Foundation of China (42277091, U22A20578), the foreign cooperation project of Fujian Province (2020I0038), the Xiamen Youth Innovation Fund Project (3502Z20206094), the FJIRSM&IUE Joint Research Fund (RHZX-2019-006), and Center for Excellence in Regional Atmospheric Environment project (E0L1B20201).

509

510

References

Belis, C. A., Pikridas, M., Lucarelli, F., Petralia, E., Cavalli, F., Calzolai, G., Berico, M., and Sciare, J.: Source apportionment of fine PM by combining high time resolution organic and inorganic chemical composition datasets, Atmos. Environ.-X, 3, 10.1016/j.aeaoa.2019.100046, 2019.

Campbell, J. R., Battaglia, M., Dingilian, K., Cesler-Maloney, M., St Clair, J. M., Hanisco, T. F., Robinson, E., DeCarlo, P., Simpson, W., Nenes, A., Weber, R. J., and Mao, J.: Source and Chemistry of Hydroxymethanesulfonate (HMS) in Fairbanks, Alaska, Environ. Sci. Technol., 10.1021/acs.est.2c00410, 2022.

Chen, G., Liu, T., Ji, X., Xu, K., Hong, Y*., Xu, L., Li, M., Fan, X., Chen, Y., Yang, C., Lin, Z., Huang, W., and Chen, J.: Source Apportionment of VOCs and O_3 Production Sensitivity at Coastal and Inland Sites of Southeast China, Aerosol Air Qual. Res., 22, 220289, 10.4209/aaqr.220289, 2022.

Chow, W. S., Liao, K., Huang, X. H. H., Leung, K. F., Lau, A. K. H., and Yu, J. Z.: Measurement report: The 10-year trend of PM2.5 major components and source tracers from 2008 to 2017 in an urban site of Hong Kong, China, Atmos. Chem. Phys., 22, 11557-11577, 10.5194/acp-22-11557-2022, 2022.

Dixon, R. W. and Aasen, H.: Measurement of hydroxymethanesulfonate in atmospheric aerosols, Atmos. Environ., 33, 2023–2029, https://doi.org/10.1016/s1352-2310(98)00416-6, 1999.

Dovrou, E., Bates, K. H., Moch, J. M., Mickley, L. J., Jacob, D. J., and Keutsch, F. N.: Catalytic role of formaldehyde in particulate matter formation, P. Natl. Acad. Sci. USA, 119, e2113265119, 10.1073/pnas.2113265119, 2022.

Feng, T., Zhao, S., Zhang, X., Wang, Q., Liu, L., Li, G., and Tie, X.: Increasing wintertime ozone levels and secondary aerosol formation in the Guanzhong basin, central China, Sci. Total Environ., 745, 10.1016/j.scitotenv.2020.140961, 2020.

Gen, M., Zhang, R., Huang, D. D., Li, Y., and Chan, C. K.: Heterogeneous SO2 Oxidation in Sulfate Formation by Photolysis of Particulate Nitrate, Environ. Sci. Technol. Letters, 6, 86-91,

536   10.1021/acs.estlett.8b00681, 2019.

537 Hong, Y., Xu, X., Liao, D., Zheng, R., Ji, X., Chen, Y., Xu, L., Li, M., Wang, H., Xiao, H., Choi, S.-D.,

538   and Chen, J.: Source apportionment of PM2.5 and sulfate formation during the COVID-19

539   lockdown in a coastal city of southeast China, Environ. Pollut., 286, 117577,

540   https://doi.org/10.1016/j.envpol.2021.117577, 2021.

541 Hong, Y., Xu, X., Liao, D., Liu, T., Ji, X., Xu, K., Liao, C., Wang, T., Lin, C., and Chen, J.: Measurement

542   report: Effects of anthropogenic emissions and environmental factors on the formation of biogenic

543   secondary organic aerosol (BSOA) in a coastal city of southeastern China, Atmos. Chem. Phys., 22,

544   7827-7841, 10.5194/acp-22-7827-2022, 2022.

545 Hong, youwei. (2023). Dataset for ACP by Hong et al., 2023 [Data set]. Zenodo. 584

546   https://doi.org/10.5281/zenodo. 7799302.

547 Hu, B., Duan, J., Hong, Y., Xu, L., Li, M., Bian, Y., Qin, M., Fang, W., Xie, P., and Chen, J.: Exploration

548   of the atmospheric chemistry of nitrous acid in a coastal city of southeastern China: results from

549   measurements across four seasons, Atmos. Chem. Phys., 22, 371-393, 10.5194/acp-22-371-2022,

550   2022.

551 Ivatt, P. D., Evans, M. J., and Lewis, A. C.: Suppression of surface ozone by an aerosol-inhibited

552   photochemical ozone regime, Nat. Geosci., 10.1038/s41561-022-00972-9, 2022.

553 Ji, X., Xu, K., Liao, D., Chen, G., Liu, T., Hong, Y. *, Dong, S., Choi, S.-D., and Chen, J.*: Spatial-

554   temporal Characteristics and Source Apportionment of Ambient VOCs in Southeast Mountain Area

555   of China, Aerosol Air Qual. Res., 22, 220016, 2022.

556 Jia, C., Tong, S., Zhang, X., Li, F., Zhang, W., Li, W., Wang, Z., Zhang, G., Tang, G., Liu, Z., and Ge,

557   M.: Atmospheric oxidizing capacity in autumn Beijing: Analysis of the O_3 and $PM_{2.5}$ episodes based

558   on observation-based model, J Environ. Sci., 124, 557-569,

559   https://doi.org/10.1016/j.jes.2021.11.020, 2023.

560 Jiang, Y., Wang, S., Xing, J., Zhao, B., Li, S., Chang, X., Zhang, S., and Dong, Z.: Ambient fine

561   particulate matter and ozone pollution in China: Synergy in anthropogenic emissions and

562   atmospheric processes, Environ. Res. Lett., 2022.

563 Kalashnikov, D. A., Schnell, J. L., Abatzoglou, J. T., Swain, D. L., and Singh, D.: Increasing co-

564   occurrence of fine particulate matter and ground-level ozone extremes in the western United States,

565   Sci. Adv., 8, 10.1126/sciadv.abi9386, 2022.

566   Li, J., Zhang, Y.-L., Cao, F., Zhang, W., Fan, M., Lee, X., and Michalski, G.: Stable Sulfur Isotopes

567   Revealed a Major Role of Transition-Metal Ion-Catalyzed SO2 Oxidation in Haze Episodes,

568   Environ. Sci. Technol., 54, 2626-2634, 10.1021/acs.est.9b07150, 2020.

569   Li, K., Jacob, D. J., Liao, H., Shen, L., Zhang, Q., and Bates, K. H.: Anthropogenic drivers of 2013-2017

570   trends in summer surface ozone in China, P. Natl. Acad. Sci. USA of the United States of America,

571   116, 422-427, 10.1073/pnas.1812168116, 2019a.

572   Li, K., Jacob, D. J., Liao, H., Zhu, J., Shah, V., Shen, L., Bates, K. H., Zhang, Q., and Zhai, S.: A two-

573   pollutant strategy for improving ozone and particulate air quality in China, Nat. Geosci., 12, 906-+,

574   10.1038/s41561-019-0464-x, 2019b.

575   Li, Y., Zhang, Z., and Xing, Y.: Long-Term Change Analysis of PM2.5 and Ozone Pollution in China's

576   Most Polluted Region during 2015-2020, Atmosphere, 13, 10.3390/atmos13010104, 2022.

577   Li, Z., Xue, L., Yang, X., Zha, Q., Tham, Y. J., Yan, C., Louie, P. K. K., Luk, C. W. Y., Wang, T., and

578   Wang, W.: Oxidizing capacity of the rural atmosphere in Hong Kong, Southern China, Sci. Total

579   Environ., 612, 1114-1122, https://doi.org/10.1016/j.scitotenv.2017.08.310, 2018.

580   Liu, T., Clegg, S. L., and Abbatt, J. P. D.: Fast oxidation of sulfur dioxide by hydrogen peroxide in

581   deliquesced aerosol particles, P. Natl. Acad. Sci. USA, 117, 1354-1359, 10.1073/pnas.1916401117,

582   2020a.

583   Liu, T., Hu, B., Yang, Y., Li, M., Hong, Y., Xu, X., Xu, L., Chen, N., Chen, Y., Xiao, H., and Chen, J.:

584   Characteristics and source apportionment of PM2.5 on an island in Southeast China: Impact of sea-

585   salt and monsoon, Atmos. Res., 235, 10.1016/j.atmosres.2019.104786, 2020.

586   Liu, T., Hong, Y., Li, M., Xu, L., Chen, J., Bian, Y., Yang, C., Dan, Y., Zhang, Y., Xue, L., Zhao, M.,

587   Huang, Z., and Wang, H.: Atmospheric oxidation capacity and ozone pollution mechanism in a

588   coastal city of southeastern China: analysis of a typical photochemical episode by an observation-

589   based model, Atmos. Chem. Phys., 22, 2173-2190, 10.5194/acp-22-2173-2022, 2022a.

590   Liu, T., Lin, Y., Chen, J., Chen, G., Yang, C., Xu, L., Li, M., Fan, X., Zhang, F., and Hong, Y.: Pollution

591   mechanisms and photochemical effects of atmospheric HCHO in a coastal city of southeast China,

592   Sci. Total Environ., 160210, https://doi.org/10.1016/j.scitotenv.2022.160210, 2022b.

593   Lou, S., Liao, H., and Zhu, B.: Impacts of aerosols on surface-layer ozone concentrations in China

through heterogeneous reactions and changes in photolysis rates, Atmos. Environ., 85, 123-138, https://doi.org/10.1016/j.atmosenv.2013.12.004, 2014.

Lu, K., Guo, S., Tan, Z., Wang, H., Shang, D., Liu, Y., Li, X., Wu, Z., Hu, M., and Zhang, Y.: Exploring atmospheric free-radical chemistry in China:the self-cleansing capacity and the formation of secondary air pollution, Nat. Sci. Rev., 6, 579-594, 2019.

Ma, T., Furutani, H., Duan, F., Kimoto, T., Jiang, J., Zhang, Q., Xu, X., Wang, Y., Gao, J., Geng, G., Li, M., Song, S., Ma, Y., Che, F., Wang, J., Zhu, L., Huang, T., Toyoda, M., and He, K.: Contribution of hydroxymethanesulfonate (HMS) to severe winter haze in the North China Plain, Atmos. Chem. Phys., 20, 5887–5897, https://doi.org/10.5194/acp-20-5887-2020, 2020.

Mitsuishi, K.; Iwasaki, M.; Takeuchi, M.; Okochi, H.; Kato, S.; Ohira, S. I.; Toda, K., Diurnal Variations in Partitioning of Atmospheric Glyoxal and Methylglyoxal between Gas and Particles at the Ground Level and in the Free Troposphere. Acs Earth and Space Chemistry 2018, 2, (9), 915-924.

Moch, J. M., Dovrou, E., Mickley, L. J., Keutsch, F. N., Cheng, Y., Jacob, D. J., Jiang, J. K., Li, M., Munger, J. W., Qiao, X. H., Zhang, Q.: Contribution of Hydroxymethane Sulfonate to Ambient Particulate Matter: A Potential Explanation for High Particulate Sulfur During Severe Winter Haze in Beijing, Geophysical Research Letters, 45, (21), 11969-11979, 2018.

Moch, J. M., Dovrou, E., Mickley, L. J., Keutsch, F. N., Liu, Z., Wang, Y., Dombek, T. L., Kuwata, M., Budisulistiorini, S. H., Yang, L., Decesari, S., Paglione, M., Alexander, B., Shao, J., Munger, J. W., and Jacob, D. J.: Global Importance of Hydroxymethanesulfonate in Ambient Particulate Matter: Implications for Air Quality, J Geophys. Res.-Atmospheres, 125, 10.1029/2020jd032706, 2020

Munger, J. W., Tiller, C., and Hoffmann, M. R.: Identification of hydroxymethanesulfonate in fog water, Science, 231, 247–249, https://doi.org/10.1126/science.231.4735.247, 1986.

Polissar, A. V., Hopke, P. K., and Paatero, P.: Atmospheric aerosol over Alaska - 2. Elemental composition and sources, J Geophys. Res.-Atmospheres, 103, 19045-19057, 10.1029/98jd01212, 1998.

Qin, Y., Li, J., Gong, K., Wu, Z., Chen, M., Qin, M., Huang, L., and Hu, J.: Double high pollution events in the Yangtze River Delta from 2015 to 2019: Characteristics, trends, and meteorological situations, Sci. Total Environ., 792, 10.1016/j.scitotenv.2021.148349, 2021.

Qu, Y., Wang, T., Yuan, C., Wu, H., Gao, L., Huang, C., Li, Y., Li, M., and Xie, M.: The underlying mechanisms of PM2.5 and O3 synergistic pollution in East China: Photochemical and heterogeneous interactions, Sci. Total Environ., 873, 162434, https://doi.org/10.1016/j.scitotenv.2023.162434, 2023.

Rienda, I. C., and Alves, C. A.: Road dust resuspension: A review, Atmos. Res., 261, 10.1016/j.atmosres.2021.105740, 2021.

Schwartz, S. E. In Mass-Transport Considerations Pertinent to Aqueous Phase Reactions of Gases in Liquid-Water Clouds, Chemistry of Multiphase Atmospheric Systems, Jaeschke, W., Ed. Springer Berlin Heidelberg: Berlin, Heidelberg, 1986; pp 415-471.

Shao, M., Yang, J., Wang, J., Chen, P., Liu, B., and Dai, Q.: Co-Occurrence of Surface O3, PM2.5 Pollution, and Tropical Cyclones in China, J Geophys. Res.Atmospheres, 127, e2021JD036310, https://doi.org/10.1029/2021JD036310, 2022.

Song, H., Lu, K., Dong, H., Tan, Z., Chen, S., Zeng, L., and Zhang, Y.: Reduced Aerosol Uptake of Hydroperoxyl Radical May Increase the Sensitivity of Ozone Production to Volatile Organic Compounds, Environ. Sci. Technol. Lett., 9, 22-29, 10.1021/acs.estlett.1c00893, 2022.

Song, S., Ma, T., Zhang, Y., Shen, L., Liu, P., Li, K., Zhai, S., Zheng, H., Gao, M., Moch, J. M., Duan, F., He, K., and McElroy, M. B.: Global modeling of heterogeneous hydroxymethanesulfonate chemistry, Atmos. Chem. Phys., 21, 457–481, https://doi.org/10.5194/acp-21-457-2021, 2021.

Vohra, K., Marais, E. A., Bloss, W. J., Schwartz, J., Mickley, L. J., Van Damme, M., Clarisse, L., and Coheur, P.-F.: Rapid rise in premature mortality due to anthropogenic air pollution in fast-growing tropical cities from 2005 to 2018, Sci. Adv., 8, eabm4435-eabm4435, 10.1126/sciadv.abm4435, 2022.

Wang, S., Zhao, Y., Chan, A. W. H., Yao, M., Chen, Z., and Abbatt, J. P. D.: Organic Peroxides in Aerosol: Key Reactive Intermediates for Multiphase Processes in the Atmosphere, Chem. Rev., 10.1021/acs.chemrev.2c00430, 2023.

Wang, W., Liu, M., Wang, T., Song, Y., Zhou, L., Cao, J., Hu, J., Tang, G., Chen, Z., Li, Z., Xu, Z., Peng, C., Lian, C., Chen, Y., Pan, Y., Zhang, Y., Sun, Y., Li, W., Zhu, T., Tian, H., and Ge, M.: Sulfate formation is dominated by manganese-catalyzed oxidation of SO2 on aerosol surfaces during haze events, Nat. Commun., 12, 10.1038/s41467-021-22091-6, 2021.

Watson, J. G., Chow, J. C., and Houck, J. E.: PM2.5 chemical source profiles for vehicle exhaust, vegetative burning, geological material, and coal burning in Northwestern Colorado during 1995, Chemo., 43, 1141-1151, 10.1016/s0045-6535(00)00171-5, 2001.

World Health Organization. WHO global air quality guidelines: particulate matter (PM2.5 and PM10), ozone, nitrogen dioxide, sulfur dioxide and carbon monoxide. 2021 (2021-12-21). ISBN 978-92-4-003422-8

Wu, X., Xu, L. L., Hong, Y. W., Chen, J. F., Qiu, Y. Q., Hu, B. Y., Hong, Z. Y., Zhang, Y. R., Liu, T. T., Chen, Y. T., Bian, Y. H., Zhao, G. Q., Chen, J. S., and Li, M. R.: The air pollution governed by subtropical high in a coastal city in Southeast China: Formation processes and influencing mechanisms, Sci. Total Environ., 692, 1135-1145, 10.1016/j.scitotenv.2019.07.341, 2019.

Wu, X., Li, M., Chen, J., Wang, H., Xu, L., Hong, Y., Zhao, G., Hu, B., Zhang, Y., Dan, Y., and Yu, S.: The characteristics of air pollution induced by the quasi-stationary front: Formation processes and influencing factors, Sci. Total Environ., 707, 10.1016/j.scitotenv.2019.136194, 2020.

Wu, Y., Huo, J., Yang, G., Wang, Y., Wang, L., Wu, S., Yao, L., Fu, Q., and Wang, L.: Measurement report: Production and loss of atmospheric formaldehyde at a suburban site of Shanghai in summertime, Atmos. Chem. Phys., 23, 2997-3014, 10.5194/acp-23-2997-2023, 2023.

Xiao, Q., Geng, G., Xue, T., Liu, S., Cai, C., He, K., and Zhang, Q.: Tracking PM2.5 and O-3 Pollution and the Related Health Burden in China 2013-2020, Environ. Sci. Technol., 56, 6922-6932, 10.1021/acs.est.1c04548, 2022.

Xu, R., Li, X., Dong, H., Lv, D., Kim, N., Yang, S., Wang, W., Chen, J., Shao, M., Lu, S., Wu, Z., Chen, S., Guo, S., Hu, M., Liu, Y., Zeng, L., and Zhang, Y.: Field observations and quantifications of atmospheric formaldehyde partitioning in gaseous and particulate phases, Sci. Total Environ., 808, 10.1016/j.scitotenv.2021.152122, 2022.

Xue, L., Gu, R., Wang, T., Wang, X., Saunders, S., Blake, D., Louie, P. K. K., Luk, C. W. Y., Simpson, I., Xu, Z., Wang, Z., Gao, Y., Lee, S., Mellouki, A., and Wang, W.: Oxidative capacity and radical chemistry in the polluted atmosphere of Hong Kong and Pearl River Delta region: analysis of a severe photochemical smog episode, Atmos. Chem. Phys., 16, 9891-9903, 10.5194/acp-16-9891-2016, 2016.

Zhang, K., Duan, Y., Huo, J., Huang, L., Wang, Y., Fu, Q., Wang, Y., and Li, L.: Formation mechanism

681   of HCHO pollution in the suburban Yangtze River Delta region, China: A box model study and

682   policy implementations, Atmos. Environ., 267, 118755, https://doi.org/10.1016/j.atmosenv.2021.118755, 2021.

684   Zhang, N., Guan, Y., Jiang, Y., Zhang, X., Ding, D., and Wang, S.: Regional demarcation of synergistic control for PM2.5 and ozone pollution in China based on long-term and massive data mining, Sci. Total Environ., 155975, https://doi.org/10.1016/j.scitotenv.2022.155975, 2022.

687   Zhao, D., Liu, G., Xin, J., Quan, J., Wang, Y., Wang, X., Dai, L., Gao, W., Tang, G., Hu, B., Ma, Y., Wu, X., Wang, L., Liu, Z., and Wu, F.: Haze pollution under a high atmospheric oxidization capacity in summer in Beijing: insights into formation mechanism of atmospheric physicochemical processes, Atmos. Chem. Phys., 20, 4575-4592, 10.5194/acp-20-4575-2020, 2020.

691   Zong, L., Yang, Y., Gao, M., Wang, H., Wang, P., Zhang, H., Wang, L., Ning, G., Liu, C., Li, Y., and Gao, Z.: Large-scale synoptic drivers of co-occurring summertime ozone and PM2.5 pollution in eastern China, Atmos. Chem. Phys., 21, 9105-9124, 10.5194/acp-21-9105-2021, 2021.